frontiers | Frontiers in Built Environment

TYPE Original Research
PUBLISHED 08 July 2024
DOI 10.3389/fbuil.2024.1394952

OPEN ACCESS

EDITED BY
Eleni N. Chatzi,
ETH Zürich, Switzerland

REVIEWED BY
Giuseppe Abbiati,
Aarhus University, Denmark
Arturo Montoya,
University of Texas at San Antonio, United States

*CORRESPONDENCE
Gastón A. Fermandois,
gaston.fermandois@usm.cl

RECEIVED 02 March 2024
ACCEPTED 03 June 2024
PUBLISHED 08 July 2024

CITATION
Quiroz M, Gálmez C and Fermandois GA (2024), Robust decentralized adaptive compensation for the multi-axial real-time hybrid simulation benchmark.
Front. Built Environ. 10:1394952.
doi: 10.3389/fbuil.2024.1394952

Robust decentralized adaptive compensation for the multi-axial real-time hybrid simulation benchmark

María Quiroz[1,2], Cristóbal Gálmez[1] and Gastón A. Fermandois[1]*

[1]Departamento de Obras Civiles, Universidad Técnica Federico Santa María, Valparaíso, Chile, [2]Department of Engineering, City, University of London, London, United Kingdom

Real-time hybrid simulation (RTHS) is a powerful and highly reliable technique integrating experimental testing with numerical modeling for studying rate-dependent components under realistic conditions. One of its key advantages is its cost-effectiveness compared to large-scale shake table testing, which is attained by selectively conducting experimental testing on critical parts of the analyzed structure, thus avoiding the assembly of the entire system. One of the fundamental advancements in RTHS methods is the development of multi-dimensional dynamic testing. In particular, multi-axial RTHS (maRTHS) aims to prescribe multi-degree-of-freedom (MDOF) loading from the numerical substructure over the test specimen. Under these conditions, synchronization is a significant challenge in multiple actuator loading assemblies. This study proposes a robust and decentralized adaptive compensation (RoDeAC) method for the next-generation maRTHS benchmark problem. An initial calibration of the dynamic compensator is carried out through offline numerical simulations. Subsequently, the compensator parameters are updated in real-time during the test using a recursive least squares adaptive algorithm. The results demonstrate outstanding performance in experiment synchronization, even in uncertain conditions, due to the variability of reference structures, seismic loading, and multi-actuator properties. Notably, this achievement is accomplished without needing detailed information about the test specimen, streamlining the procedure and reducing the risk of specimen deterioration. Additionally, the tracking performance of the tests closely aligns with the reference structure, further affirming the excellence of the outcomes.

KEYWORDS

real-time hybrid simulation, multiple actuators, adaptive compensation, decentralized control, dynamic coupling, benchmark

1 Introduction

Real-time hybrid simulation (RTHS) is a powerful and highly reliable technique that integrates experimental testing with numerical modeling (Nakashima et al., 1992). As a real-time variant of pseudo-dynamic testing, RTHS enables studying rate-dependent components under realistic conditions. One of its key advantages is its cost-effectiveness, which is achieved by selectively conducting experimental testing on critical parts of the analyzed structure, thus avoiding the assembly of the entire system. The laboratory essays primarily focus on the experimental substructure, while the well-known portions are accurately represented through numerical modeling within a computer

interface. This innovative approach offers a practical and efficient means of evaluating structural behavior and performance, making RTHS a valuable tool for various engineering applications (Asai et al., 2013; Botelho and Christenson, 2014; Ghaffary and Mohammadi, 2019).

In RTHS, actuators are typically utilized to impose the numerical response over the experimental parts. Simultaneously, the experimental forces are measured and fed back into the numerical substructure. However, the procedure must enforce real-time compatibility and equilibrium at the hybrid interface (Dermitzakis and Mahin, 1985). Therefore, seamless synchronization between the numerical and experimental components demands meticulous time management to avoid inaccurate and unstable responses (Horiuchi et al., 1996). Several challenges arise in this process, including the time required for calculations, the precise application of displacements using actuators, and the digital acquisition of measured forces within extremely small time increments. As a consequence, researchers have developed control techniques to compensate for the actuator's dynamics and minimize tracking errors to address the synchronization challenge. Early methods are based on polynomial extrapolation, assuming a constant delay (Horiuchi et al., 1999). Other methods are based on the inverse of the first-order transfer function, which represents the transfer system (Chen and Ricles, 2010). Models with higher-order transfer functions are used for model-based techniques (Carrion and Spencer, 2007). Model-based feedforward and feedback compensation (Phillips and Spencer Jr, 2012) have excellent results if a good plant model is available to design the controller. However, there are no guarantees of accuracy or stability when significant uncertainty exists in the model.

An alternative to traditional dynamic compensators is the adaptive compensation algorithm, which has been proposed to address the uncertainty or significant non-linearity in the control plant. Some of them use a first-order transfer function with adapting parameters to represent the transfer system, where the adaptation depends on a frequency-domain evaluation index (FEI) analysis of commanded and measured signals, such as adaptive phase-lead compensation (Tao and Mercan, 2019) or windowed FEI compensation (Xu et al., 2019). Other methods, like adaptive time series (Chae et al., 2013) and conditional adaptive time series (Palacio-Betancur and Gutierrez Soto, 2019), estimate the plant through Taylor series expansion and adjust the parameters in the time domain. Adaptive model-based compensation (Chen et al., 2015) consists of an estimate of the plant in the frequency domain; then, compensation is implemented in the time domain using numeric derivatives of the commanded signal and adaptation based on the gradient. Wang et al. (2020) used adaptive delay compensation based on a discrete system model where the compensation commands are generated using the target, measured, and previous displacements. Ning et al. (2020) used an adaptive model-based control strategy with feedforward and feedback control and added a Kalman filter for parameter estimation.

The necessity of carrying out realistic experiments has been the principal factor that led to the development of multi-dimensional testing in RTHS, giving way to multi-axial RTHS (maRTHS). These tests prescribe multiple-degree-of-freedom (MDOF) responses from the numerical substructure into the test specimen, which requires multiple hydraulic actuators to prescribe all the motions over the experimental substructure (Fermandois and Spencer, 2017). As the complexity of the problem increases, enforcing a higher number of degrees of freedom (DOFs) at a given interface boundary condition may require incorporating supplementary physical components or multi-axial loading systems, such as high-stiff links or couplers. The assemblage of multi-axial hydraulic actuators demands nonlinear coordinate transformations, adding complexity due to nonlinearities, uncertainties, and internal coupling, among other complexities. Consequently, conducting experiments with such multi-axial setups and achieving precise synchronization remain a considerable challenge, making developing and validating effective multiple-input multiple-output (MIMO) control strategies urgently necessary (Najafi et al., 2023). Moreover, most of the previously mentioned compensation algorithms have been tested only on single-actuator problems (Silva et al., 2020).

Meanwhile, the compensation algorithms in RTHS predominantly use displacement control. Two primary real-time control approaches are employed for multi-actuator devices: centralized and decentralized (Najafi et al., 2023). The former adopts a more comprehensive approach concerning the interaction between actuators, treating multiple actuator loading platforms as MIMO systems in Cartesian coordinates and addressing system-wide actuator dynamics (Fermandois and Spencer, 2017). However, the design and implementation of centralized controllers can pose challenges due to the many parameters requiring fine-tuning. On the contrary, decentralized control is preferred due to its comparatively simple design, enabling dynamic compensators initially crafted for single-input, single-output systems in actuator coordinates (Najafi et al., 2020). However, it should be noted that such controllers may exhibit limitations when grappling with experiments characterized by significant multi-actuator and specimen dynamic coupling.

Hence, this study proposes a robust and decentralized adaptive compensation (RoDeAC) method for maRTHS experimental tests and is developed and validated through the next-generation maRTHS benchmark problem (Condori et al., 2023). The proposed method can be designed independently from the experimental substructure, avoiding unnecessary initial identification testing that may cause premature damage to the physical specimens before the maRTHS test. By incorporating adaptation over the compensation layer, this technique maintains excellent synchronization even in the presence of uncertain and time-varying properties of the specimen. We propose defining the initial conditions and parameters of the controller using only knowledge of the transfer system through a model of the multi-actuator loading assembly, including the interaction with the test specimen. The initial calibration of the controller is carried out through offline simulations, where the decentralized multi-actuator is trained with assumed perturbed structural loading and coupling values.

This study is structured as follows: Section 2 presents the problem formulation corresponding to the virtual maRTHS benchmark problem. Section 3 describes the methodology employed to compensate the actuators involved in maRTHS using a recursive least squares (RLS) adaptive compensator. Section 4 details the initial calibration of RoDeAC for the benchmark problem. Section 5 provides the results of the

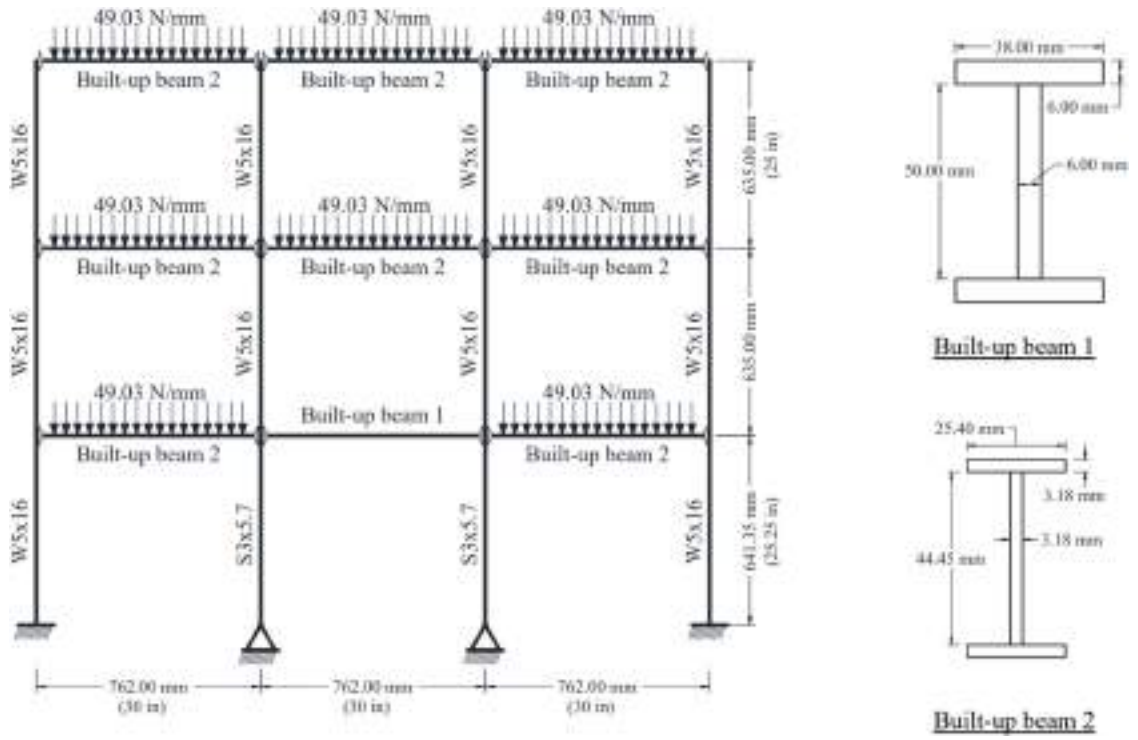

FIGURE 1
Reference structure considered for the maRTHS benchmark problem (Condori et al., 2023).

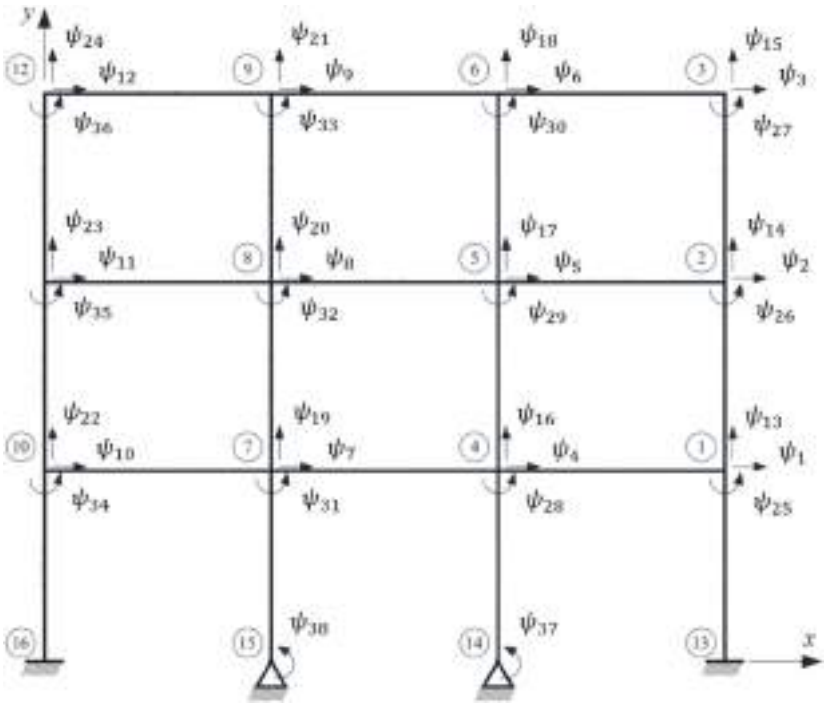

FIGURE 2
Numeration of DOF of the reference structure (adapted from Condori et al., 2023).

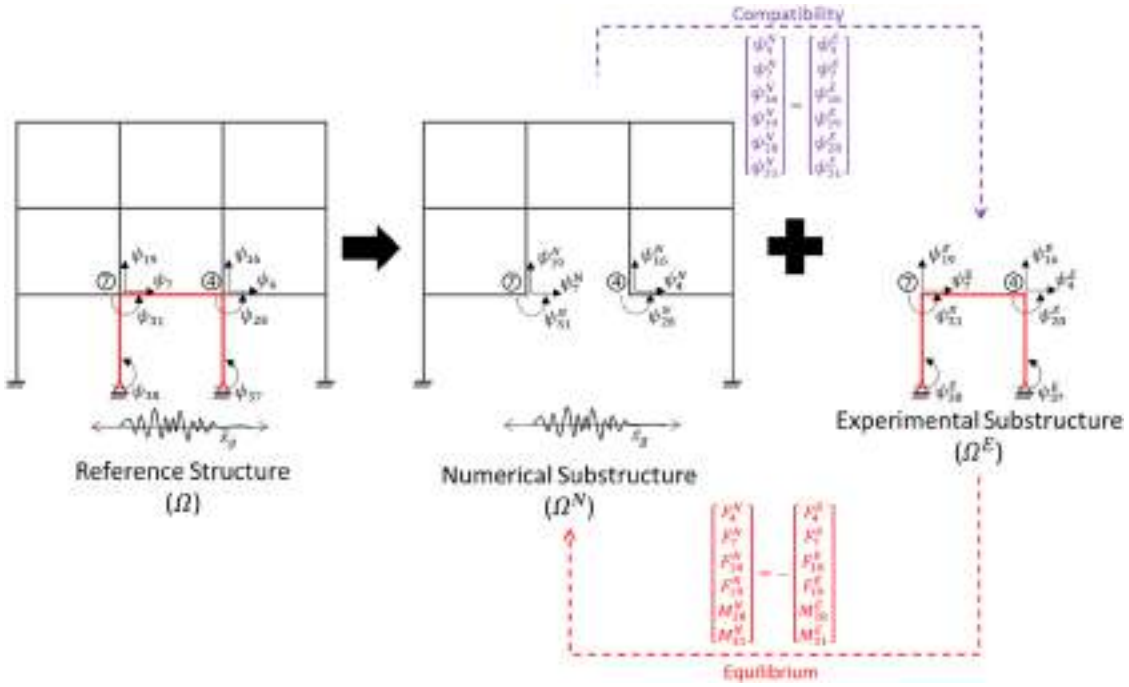

FIGURE 3
Partition considered for the maRTHS benchmark problem. (adapted from Condori et al., 2023).

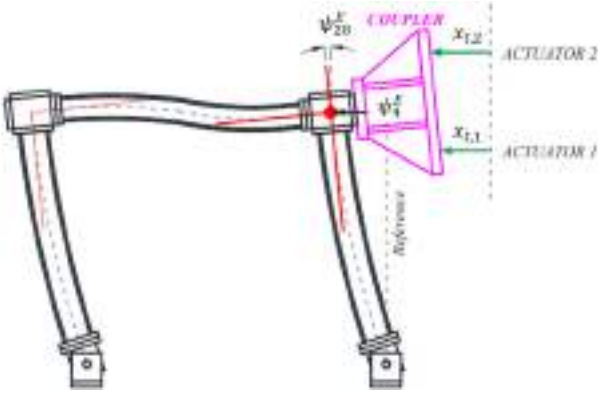

FIGURE 4
Description of the experimental setup employed for the maRTHS benchmark problem (adapted from Condori et al., 2023).

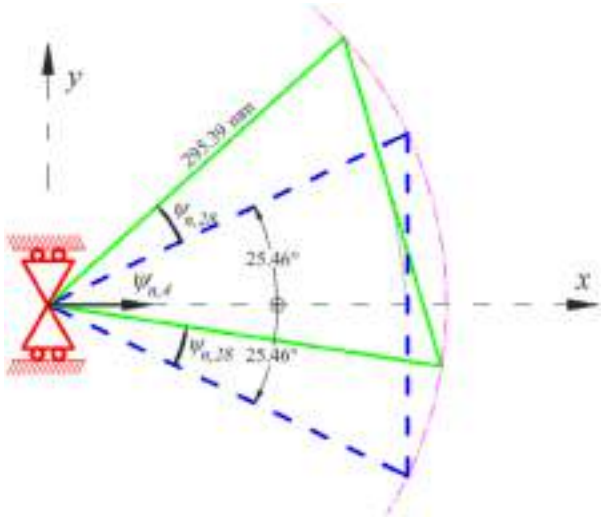

FIGURE 5
Rigid coupler kinematics (adapted from Condori et al., 2023).

numerical simulations and their comparisons regarding the benchmark. Finally, Section 6 discusses the principal findings and final remarks of this study.

2 Problem description

2.1 Reference structure

The maRTHS benchmark problem (Condori et al., 2023) is considered in this study for the development and validation of a proposed robust compensation algorithm that is capable of rejecting uncertainties mainly due to specimen-multiactuator interactions. In this benchmark problem, a three-story, three-bay, planar steel moment frame is chosen as the reference structure, as shown in Figure 1. Steel shapes and tributary gravity loads are provided to compute masses for dynamic transient analyses.

A multi-degree-of-freedom (MDOF) linear-time-invariant (LTI) numerical model is provided for the reference structure. The structural system has linear-elastic behavior and three degrees of freedom (DOFs) per node: two translational DOFs

TABLE 1 Parameter uncertainty definition (Condori et al., 2023).

Component (see Eq. 10)	Parameter	Nominal value (μ)	Standard deviation (σ)
$\frac{num_{11}(s)}{den_{11}(s)}$ and $\frac{num_{21}(s)}{den_{21}(s)}$	Zero 1	−753.98	41.47
	Zero 2	−565.48	31.1
	Pole 1	−16.65	1.00
	Pole 2	−251.32	15.08
$\frac{num_{12}(s)}{den_{12}(s)}$ and $\frac{num_{22}(s)}{den_{22}(s)}$	Zero 1	−18.85	0.57
	Zero 2	−31.42	0.94
	Pole 1	−21.99	0.66
	Pole 2	−116.24	−3.49
$\frac{num_{es}(s)}{den_{es}(s)}$	Pole 1 and 2	−314.16 ± 395.84i	15.71 + 19.79i

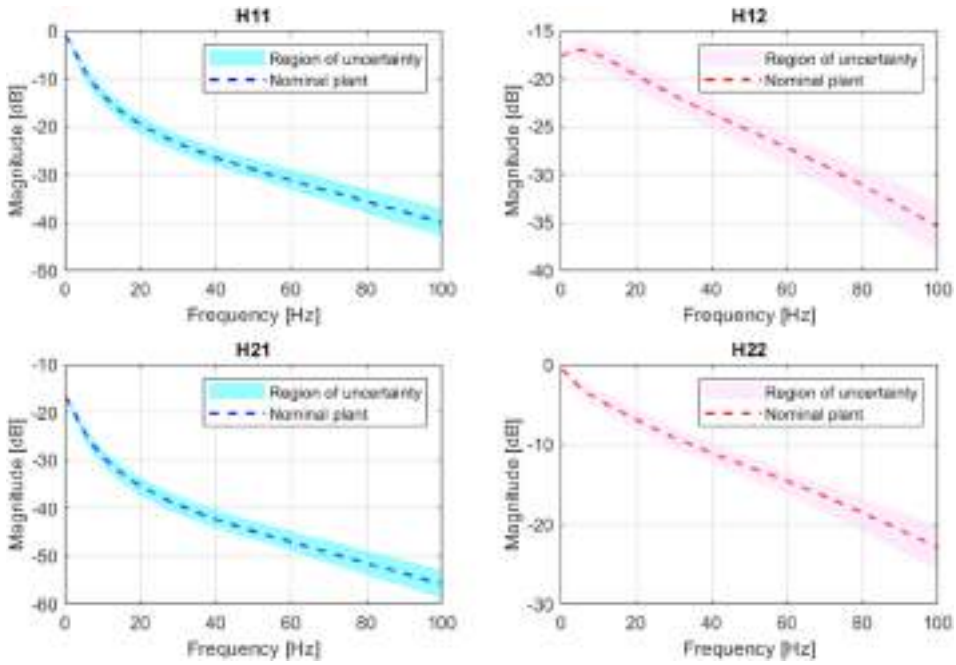

FIGURE 6
FRF regions for the plant model uncertainty. (adapted from Condori et al., 2023).

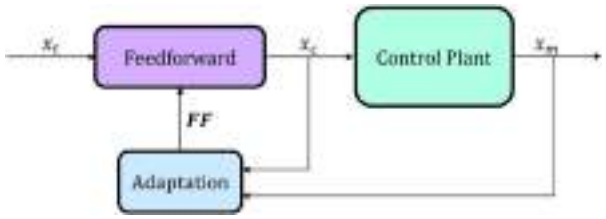

FIGURE 7
Main architecture of RLS adaptive compensation.

along the global x- and y-axes and one rotational DOF θ around the z-axis, perpendicular to the xy-plane. Therefore, the total number of DOFs in this model is 38, arranged in a displacement vector ψ according to the numeration in Figure 2, i.e., $\psi = [\psi_1 \dots \psi_{38}]^T$. Numeration begins with the horizontal displacements, followed by the vertical displacements, and finally, the rotations of each node. Moreover, only seismic loading in the horizontal direction is considered for this maRTHS study (i.e., no gravity loads are applied over the structural system).

The equation of motion (EOM) is given by Eq. 1:

$$M\ddot{\psi} + C\dot{\psi} + K\psi = -M\Gamma\ddot{x}_g, \tag{1}$$

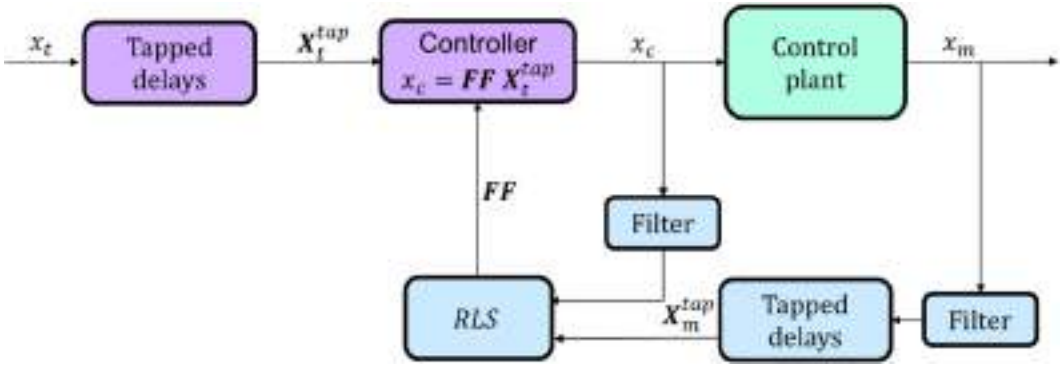

FIGURE 8
Flowchart of the RLS adaptive compensator.

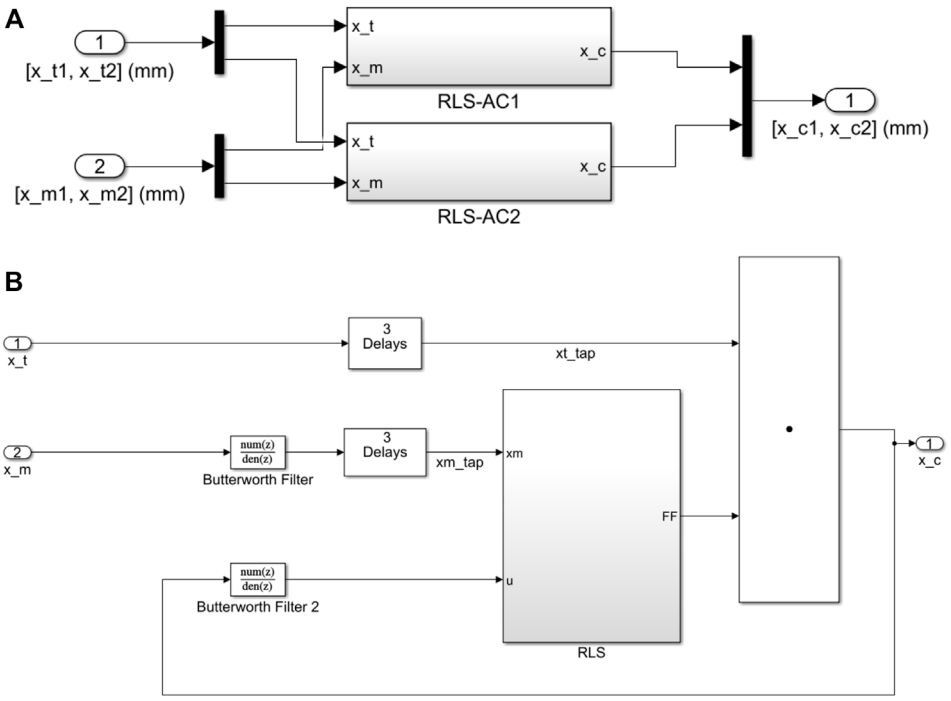

FIGURE 9
Block diagram of the RoDeAC in actuator coordinates: **(A)** maRTHS implementation and **(B)** subsystem considered for each actuator.

where M, C, and K are the mass, damping, and stiffness matrices of the reference structure, respectively. Γ is an influence vector that describes the inertial effects of the seismic excitation on the masses of the system, where a value of one is defined in the horizontal directions (i.e., the direction of the ground motion) and zero in the rest. $\ddot{x}_g$ is a scalar function associated with the ground acceleration in the x-direction. Finally, $\ddot{\psi}$, $\dot{\psi}$, and ψ are the relative acceleration, velocity, and displacement vectors with respect to the ground for each DOF, respectively. Initial rest conditions are considered for this problem (i.e., $\psi_i(0) = \dot{\psi}_i(0) = 0$, where $i = [1, 38]$).

As a consequence, the first five natural frequencies are $f_1 = 2.29$ Hz, $f_2 = 12.74$ Hz, $f_3 = 26.28$ Hz, $f_4 = 26.53$ Hz, and $f_5 = 29.91$ Hz. Meanwhile, the damping matrix is calculated using the Rayleigh damping method with a damping ratio of 5% specified for the first and third modes, assumed to be proportional to the sum of the mass and stiffness matrices of the reference system.

2.2 Substructuring

In the context of RTHS, instead of solving the EOM for the entire reference domain, a process known as *substructuring* can be employed to subdivide the domain into smaller subdomains, such that the order of large and complex structural systems is reduced for efficient computations

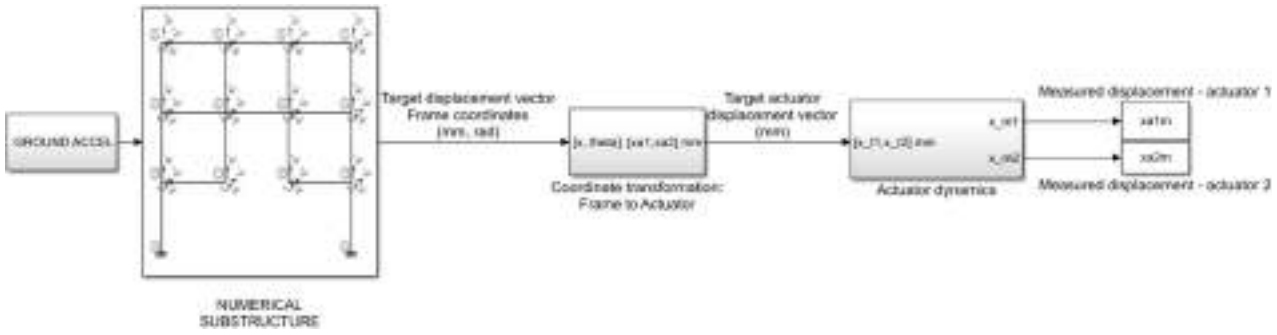

FIGURE 10
Block diagram of the offline calibration testing.

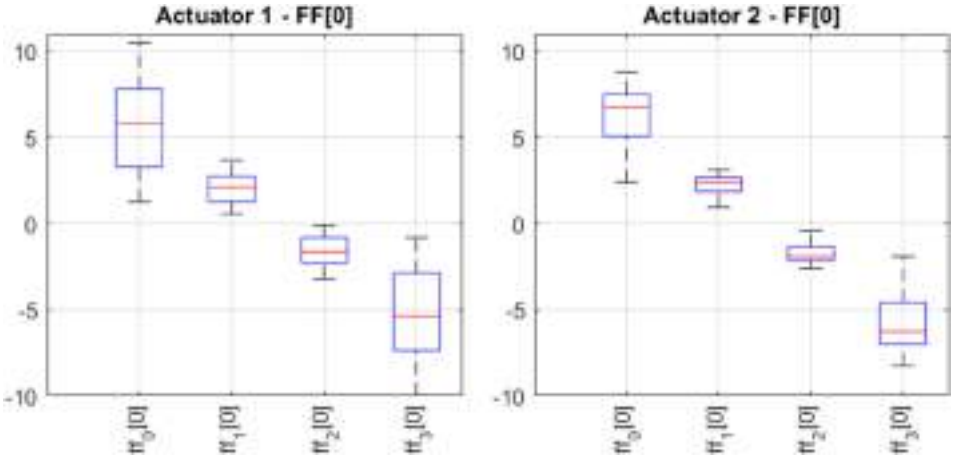

FIGURE 11
Statistical dispersion of the initial values for parameter *FF*[0] of RoDeAC for different earthquake ground motions and seismic intensity measures.

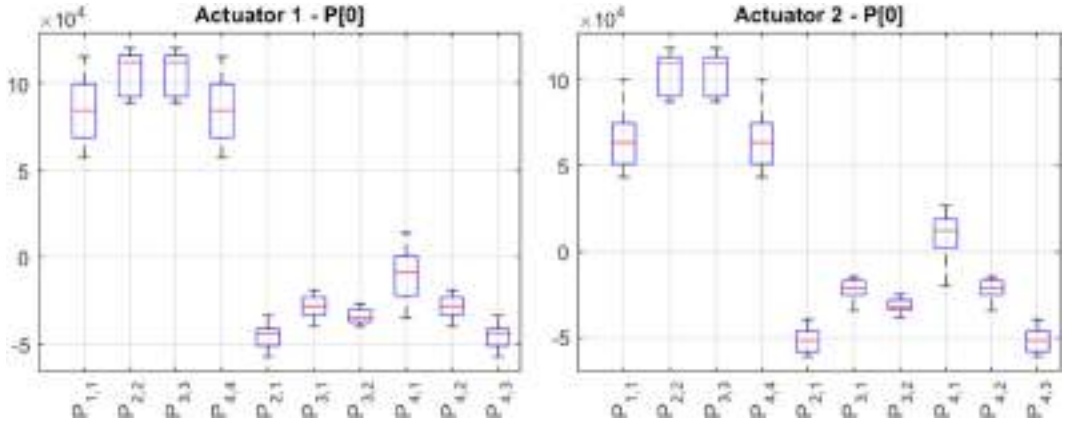

FIGURE 12
Statistical dispersion of the initial values for parameter *P*[0] of RoDeAC for different earthquakes and intensity measures. (Note: *P*[0] is symmetric, so only non-redundant values are shown.).

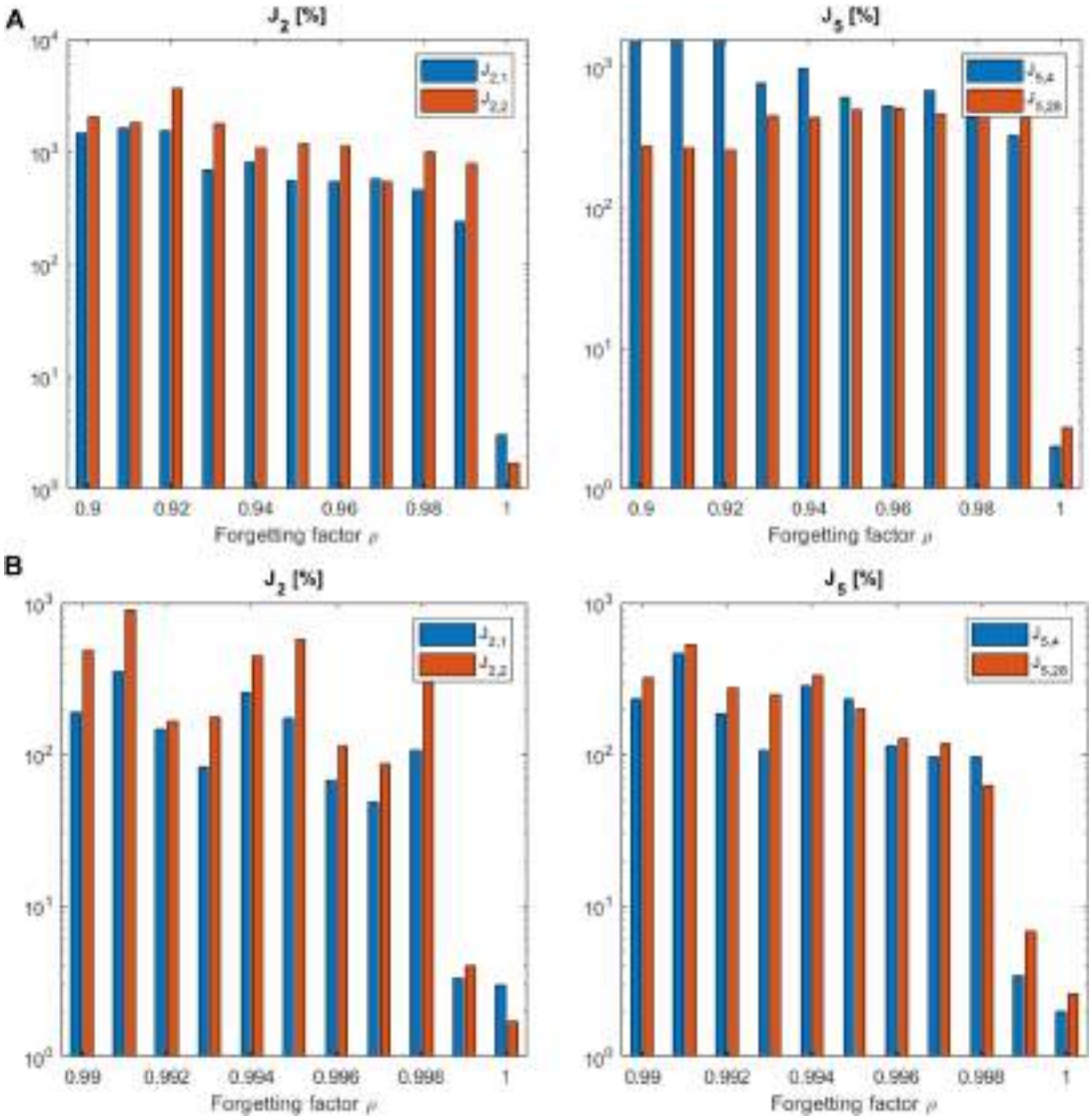

FIGURE 13
Influence of the forgetting factor on the performance of virtual maRTHS, ranging from **(A)** 0.9 to 1; and **(B)** 0.99 to 1.

(Dermitzakis and Mahin, 1985). Each subdomain can be solved independently, provided that coupling between components is enforced through compatibility and equilibrium conditions at their interfaces.

In the benchmark case, the domain is decomposed into two non-overlapping subdomains, i.e., $\Omega = \Omega^N \cup \Omega^E$, where Ω^N is called the numerical substructure and Ω^E is the experimental substructure, as shown in Figure 3. The first-story central frame is selected as the experimental substructure, which is assumed to be the less-understood part of the entire structure.

If we assume the frame exhibits linear elastic behavior, the matrices for partitioned mass, damping, and stiffness can be expressed as the combination of numerical components (denoted with the superscript "N") and experimental components (denoted with the superscript "E"): as shown in Eqs 2, 3:

$$(M^N + M^E)\ddot{\psi} + (C^N + C^E)\dot{\psi} + (K^N + K^E)\psi = -M\Gamma\ddot{x}_g, \quad (2)$$

$$M = M^N + M^E,\ C = C^N + C^E,\ K = K^N + K^E. \quad (3)$$

The terms associated with the experimental substructure can be arranged into the right-hand side of the EOM as described in Eqs 4, 5:

$$M^N\ddot{\psi} + C^N\dot{\psi} + K^N\psi = -M\Gamma\ddot{x}_g - f^E, \quad (4)$$

$$f^E = M^E\ddot{\psi} + C^E\dot{\psi} + K^E\psi. \quad (5)$$

Here, f^E is the feedback force vector produced by the experimental substructure during the dynamic testing, directly measured or estimated using measured data from the experimental domain.

Due to boundary conditions, both compatibility and equilibrium must be satisfied, as mentioned previously in this section. The first condition assures that the displacements at the interface of the subdomains are the same, allowing maRTHS to impose the numerical displacements (and their time derivatives) into the

experimental substructure. In this case, they are given by the following DOFs: $\psi^N = [\psi_4^N \ \psi_7^N \ \psi_{16}^N \ \psi_{19}^N \ \psi_{28}^N \ \psi_{31}^N]^T$. The second condition establishes the relationship between the numerical and experimental forces as their sum at the interface must equal zero (i.e., force equilibrium). Then, in maRTHS, the generated physical restoring forces $f^E = [F_4^E \ F_7^E \ F_{16}^E \ F_{19}^E \ M_{28}^E \ M_{31}^E]^T$ are measured and fed back to the numerical substructure. Both conditions are illustrated in Figure 3.

In maRTHS, the previously mentioned process is repeated until the simulation reaches the final simulation time t_f, with real-time constraints. In that regard, Figure 3 can be considered the ideal maRTHS since there are no additional components such as hydraulic actuators, inertial effects (e.g., the mass of loading connectors), or measured signals contaminated with high-frequency noise. In an actual RTHS implementation, the experimental substructure is physically built and connected to the numerical substructure through a *transfer system* (i.e., loading assembly) to ensure dynamic synchronized motion at the substructure interface nodes during the real-time experiment. The insertion of the transfer system in the experimental domain changes the dynamic properties of the experimental substructure, and a control approach must be included to compensate for these added dynamic and other negative effects. The virtual simulation of this realistic computational implementation is called virtual RTHS (vRTHS), which is considered the closest realization of an actual RTHS for training and development purposes.

In this benchmark problem, the EOM is integrated using the fourth-order Runge–Kutta integration scheme incorporated in Simulink (ode4), and the sampling frequency F_s is fixed at 1024 Hz.

2.3 Transfer system

In this section, we explain the transfer system, which consists of a set of servo-hydraulic actuators. First, the vertical DOFs along the global coordinate y are ignored due to their insignificant values compared to the horizontal displacements. The main reason for this assumption is the negligible axial deformations in columns since gravity loads are not incorporated in the maRTHS simulation and columns show high axial stiffness. On the other hand, due to experimental setup limitations, only the boundary conditions for node 4 of the experimental substructure are prescribed and implemented in the maRTHS benchmark problem. Therefore, only two actuators provide translational and rotational motion to node 4 of the experimental substructure with the aid of a coupler system. The experimental setup is shown in Figure 4, assembled in the Intelligent Infrastructure Systems Laboratory (IISL) at Purdue University (Condori et al., 2023). It should be noted that DOF ψ_{16}, which represents the vertical displacement of node 4, has been excluded from this study, as elucidated earlier, and consequently is not depicted in Figure 4. In addition, node 7 DOFs should be measured in practice. However, in this virtual implementation, they are estimated from the ideal properties of the experimental substructure and the estimated node 4 DOFs from the displacements of the actuators.

The servo-hydraulic actuators are Shore Western 910D series, with a nominal force capacity of 9.34 kN and a stroke of ±63 mm, with a built-in linear variable differential transformer (LVDT) transducer that collects measurements of linear displacements, and two load cells (Interface, 1000 series) with a nominal force capacity of 11.2 kN, providing instantaneous force measurements. These hydraulic actuators operate with a hydraulic power supply (MTS pump) with a capacity of up to 680 L/min at 206 Bar. Meanwhile, the coupler, made from SAE 1018 low-carbon steel plates, has a mass of 17.9 kg. Furthermore, it is worth mentioning that the benchmark problem statement does not explicitly report the moment of inertia with respect to the center of mass of the coupler since it is assumed that these inertial effects were indeed incorporated when they conducted system identification of the control plant (i.e., transfer system connected to the test specimen).

2.3.1 Coupler coordinate transformation

The actuators enforce translations into the physical specimen. Therefore, a coordinate transformation is required between the translational and rotational DOFs of the numerical substructure in Cartesian coordinates and the displacements on actuator coordinates. The following four important assumptions are made:

i. The coupler deformations are negligible (i.e., rigid body motion).
ii. The vertical motion of the nodes is neglected.
iii. The rotations of the column-beam joints are small because the behavior of the frame is limited to linear elasticity.
iv. The connection of the coupler to the column-beam joint provided by the high-strength bolts is rigid; hence, the deformations are negligible.

Figure 5 shows the kinematics of the rigid coupler, illustrated by the blue dashed triangle in the default position and with a green continuous triangle for finite rotations. Considering the geometry shown in Figure 5, the coordinate transformation can be calculated from Eq. 6:

$$\begin{bmatrix} x_{t,1} \\ x_{t,2} \end{bmatrix} = \psi_4^N \begin{bmatrix} 1 \\ 1 \end{bmatrix} + 295.39 \begin{bmatrix} \cos\left(\psi_{28}^N - \frac{25.46\pi}{180}\right) - \cos\left(-\frac{25.46\pi}{180}\right) \\ \cos\left(\psi_{28}^N + \frac{25.46\pi}{180}\right) - \cos\left(\frac{25.46\pi}{180}\right) \end{bmatrix}, \tag{6}$$

where $[x_{t,1} \ x_{t,2}]^T$ are the target displacements obtained from the geometric transformations of the numerical substructure, $[x_{m,1} \ x_{m,2}]^T$ are the actual displacements from each actuator, where subscript 1 and 2 represent the bottom and top actuators, respectively (hence, they are in "actuator coordinates").

Meanwhile, $\hat{\psi}_4$ and $\hat{\psi}_{28}$ are the estimated DOFs of translation and rotation of node 4 in frame coordinates from the geometric transformations of the measured actuator displacements $[x_{m,1} \ x_{m,2}]^T$ provided in Eqs 7, 8:

$$\hat{\psi}_{28} = \left[\frac{x_{m,1} - x_{m,2}}{2 \times 295.39 \sin\left(\frac{25.46\pi}{180}\right)}\right], \tag{7}$$

$$\hat{\psi}_4 = x_{m,1} - 195.39\left[\cos\left(\hat{\psi}_{28} - \frac{25.46\pi}{180}\right) - \cos\left(\frac{25.46\pi}{180}\right)\right]. \tag{8}$$

2.3.2 Control plant dynamics

The control plant (i.e., transfer system + specimen) has two inputs $[x_{c,1}\ x_{c,2}]^T$ and two outputs $[x_{m,1}\ x_{m,2}]^T$ representing the control inputs and measured displacements, respectively. Therefore, a compact 2 × 2 transfer matrix description of the control plant is convenient, as expressed in Eq. 9:

$$H = \begin{bmatrix} H_{11} & H_{12} \\ H_{21} & H_{22} \end{bmatrix}, \tag{9}$$

where H_{ij} is the transfer function for output i, given input j. The diagonal terms describe the direct relationship between the input and output of a specific actuator when this is commanded. In contrast, the off-diagonal terms provide the internal coupling behavior of one actuator when the other is commanded. Therefore, the control plant is rewritten in Eq. 10:

$$H = \begin{bmatrix} \frac{num_{11}(s)}{den_{11}(s)} & \frac{num_{12}(s)}{den_{12}(s)} \\ \frac{num_{21}(s)}{den_{21}(s)} & \frac{num_{22}(s)}{den_{22}(s)} \end{bmatrix} \cdot \frac{num_{es}(s)}{den_{es}(s)}, \tag{10}$$

where $\frac{num_{ij}(s)}{den_{ij}(s)}$ represents the numerator and denominator of the transfer function H_{ij} and $\frac{num_{es}(s)}{den_{es}(s)}$ characterizes the poles and zeros of the frame (experimental substructure).

The nominal values for the transfer function parameters of Eq. 10 are identified using experimental data using four spectral densities of band-limited white noise (BLWN) signals as inputs to the control plant. The first two tests were implemented using a 0–100 Hz BLWN signal to only one of the actuators while setting zero for the other one, thus allowing the calculation of the columns of the experimental transfer matrix. Then, a two-pole transfer function model is fitted to the experimental frequency response functions (FRFs) (Condori et al., 2023). Then, transfer function parameters are modeled as random variables with a normal distribution to consider uncertainty in the system (e.g., geometry, material properties, eccentricity, and nonlinearities). Random variations in the poles and zeros of the nominal plant model generate these differences by introducing changes from a standard normal distribution sampling process, which creates a family of FRFs where any FRF member represents a potential control plant. Finally, the nominal values and standard deviation of each parameter are presented in Table 1 and drawn in Figure 6.

3 Methodology

3.1 Recursive least squares adaptive compensation

In this study, the recursive least squares adaptive compensation (RLS-AC) initially proposed by Galmez and Fermandois (2022) for maRTHS systems is considered for application in the context of the maRTHS benchmark problem to provide a detailed comparison in terms of its performance and robustness with the benchmark results. The compensation is employed in a decentralized manner for reference tracking of multiple actuators in maRTHS. In this way, each actuator is treated as an independent control plant, and the goal of each compensator is to minimize the tracking error between a target signal x_t and the measured signal x_m for a single actuator, i.e., $e = |x_m - x_t| \approx 0$.

The RLS-AC technique consists of the design of two fundamental components: (i) a feedforward compensator, responsible for reference-tracking performance; and (ii) a recursive parameter estimator, which aims to provide sufficient robustness to the closed-loop system under unwanted disturbances and measurement noises. Both the feedforward and parameter estimators are designed independently, based on the nominal control plant model defined in Section 2.3. A schematic representation of the RLS-AC architecture employed in RTHS is presented in Figure 7.

In this study, three discrete-time signals are considered in the RLS-AC architecture: (i) target signal $x_t[i]$ coming from the numerical substructure; (ii) command signal $x_c[i]$ that is generated from a feedforward controller and applied to the control plant; and (iii) measured signal $x_m[i]$ from the control plant, including the specimen-actuator interaction and sensor noise. Note that the relationship between continuous and discrete time is given by $t_i = iT_s$, where i is the discrete-time index and $T_s = 1/F_s$ is the sampling time. The adaptation process is made through four adaptive parameters represented by the vector $FF[i] = \{ff_0[i] \quad ff_1[i] \quad ff_2[i] \quad ff_3[i]\}$. Thus, the RLS-AC cost function is built considering only four tapped delays of the present time signals. Indeed, sampling time and size in RLS-AC may have an influence on the performance of the controller. However, this study does not consider the effects of different sampling times and sizes on the adaptive parameters' evolution.

Here, the command signal to the actuator can be obtained from the Eq. 11:

$$\begin{aligned} x_c[i] &= FF[i]X_t^{tap}[i] \\ &= \{ff_0[i] \quad ff_1[i] \quad ff_2[i] \quad ff_3[i]\}\begin{Bmatrix} x_t[i] \\ x_t[i-1] \\ x_t[i-2] \\ x_t[i-3] \end{Bmatrix}, \end{aligned} \tag{11}$$

where $x_c[i]$ is the command signal at the time step i, $FF[i]$ are the adaptive parameters updated during the test with a recursive least squares (RLS) method (Söderström and Stoica, 1988), and $X_t^{tap}[i] = \{x_t[i] \quad x_t[i-1] \quad x_t[i-2] \quad x_t[i-3]\}^T$ are the tapped target displacements. The parameters $FF[i]$ are updated using the adaptation law provided in Eqs 12, 13:

$$FF[i] = FF[i-1] + \left(\frac{P[i-1]X_m^{tap}[i]}{\rho + X_m^{tap}[i]^T P[i-1] X_m^{tap}[i]}\right)e[i], \tag{12}$$

$$e[i] = x_c[i] - FF[i]X_m^{tap}[i], \tag{13}$$

where $X_m^{tap}[i]$ is the tapped measured displacement, $e[i]$ is the compensator error, ρ is the forgetting factor (see Section 4.2), and $P[i]$ is the 4×4 covariance matrix, which is updated according to the difference equation in Eq. 14:

$$P[i] = \frac{1}{\rho}\left\{I - \left(\frac{P[i-1]X_m^{tap}[i]}{\rho + X_m^{tap}[i]^T P[i-1] X_m^{tap}[i]}\right)X_m^{tap}[i]^T\right\}P[i-1], \tag{14}$$

where I is the 4×4 identity matrix.

The initial adaptive parameter $FF[0]$ and covariance matrix $P[0]$ must be defined to initialize the RLS method. A standard least-

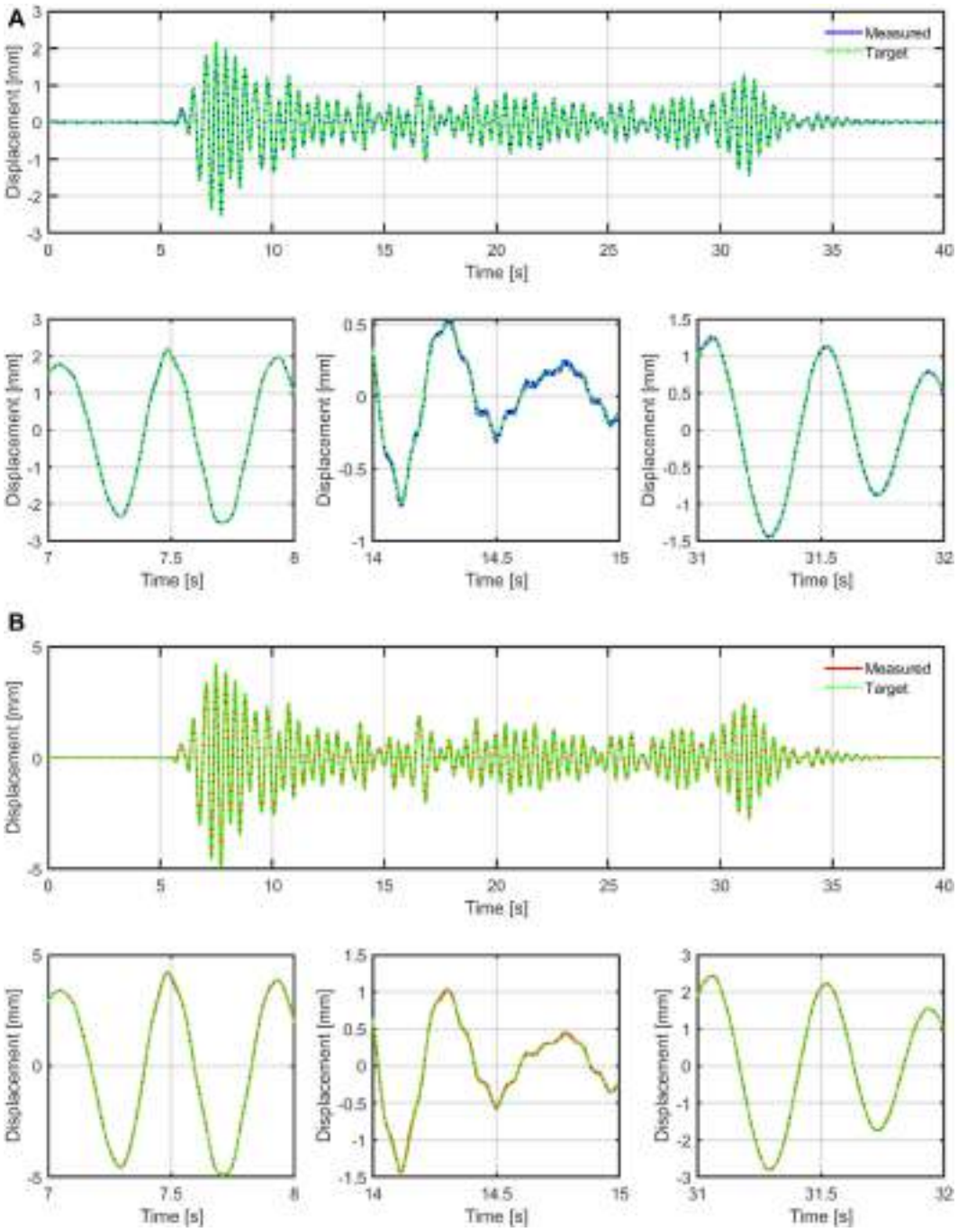

FIGURE 14
maRTHS tracking performance in actuator coordinates. Target and measured actuator displacement for **(A)** actuator 1 and **(B)** actuator 2.

squares method with offline test data is employed to evaluate the initial parameters according to Söderström and Stoica (1988) and Wang et al. (2020), as described in Eqs 15–18:

$$P[0] = \left(\Phi^T\Phi\right)^{-1}, \tag{15}$$

$$FF[0] = \left(\Phi^T\Phi\right)^{-1}\Phi^T Y, \tag{16}$$

$$\Phi = \left[X_m^{tap}[1], X_m^{tap}[2], \ldots, X_m^{tap}[L]\right]^T, \tag{17}$$

$$Y = \left[x_t[1], x_t[2], \ldots, x_t[L]\right]^T, \tag{18}$$

where L indicates the length of the data sequence employed for the initial calibration. To obtain the offline test data, one can evaluate and impose the response of the numerical substructure on the control plant, with or without a specimen. In addition, a fourth-order Butterworth filter with a cut-off frequency of 20 Hz is chosen for noise rejection. Note that the associated time delay only affects the adaptation process and does not affect compensation directly. The previously mentioned process is schematized in Figure 8.

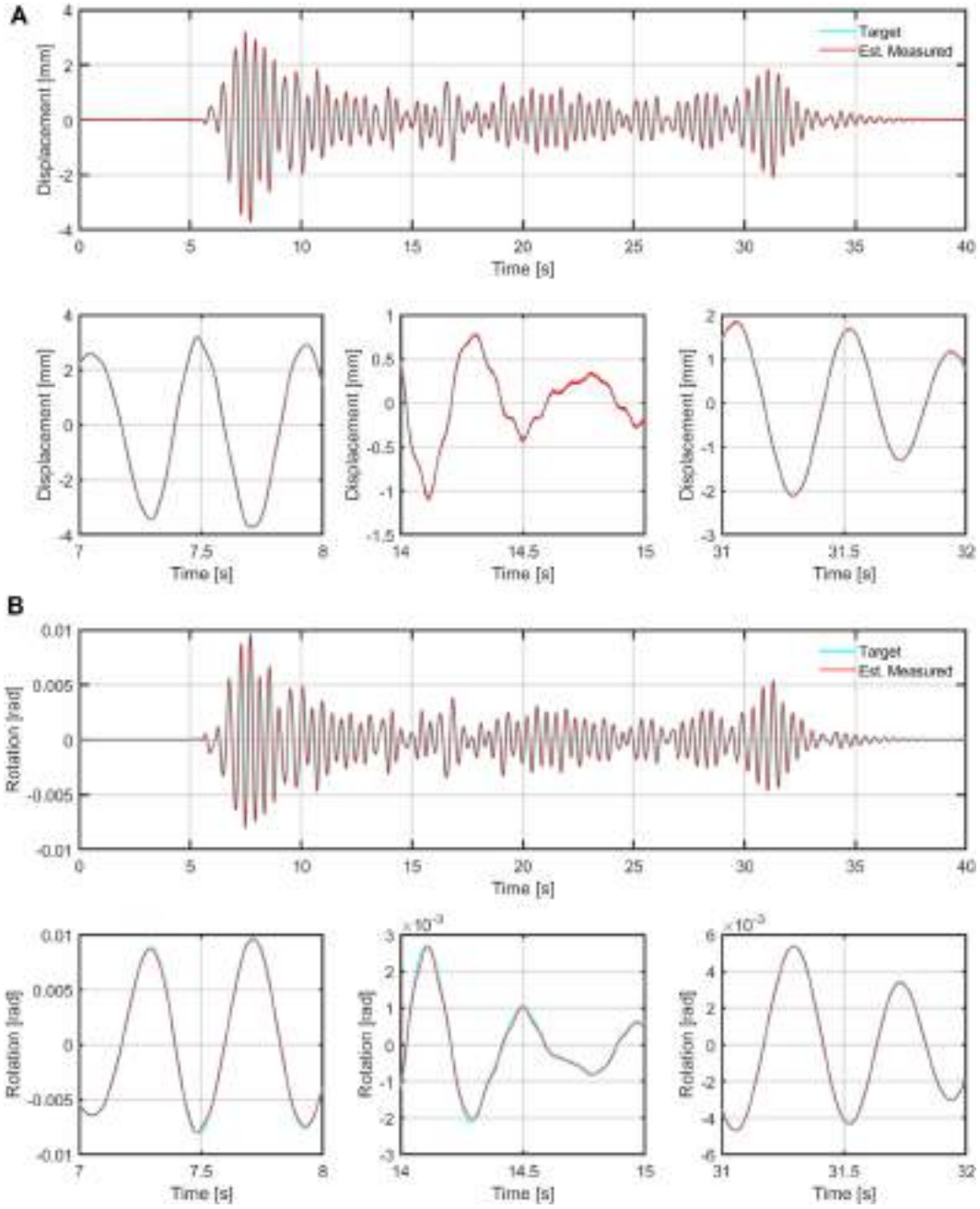

FIGURE 15
maRTHS tracking performance at the interface node (frame coordinates). Target numerical substructure vs. estimated experimental responses for **(A)** translational DOF (ψ_4) and **(B)** rotational DOF (ψ_{28}).

3.2 Decentralized adaptive compensator for maRTHS testing

The algorithm mentioned before is applied to each actuator in a decentralized manner; this means that for each actuator, there is a different compensator that works independently from each other, with unique initial parameters and adaptation processes, as shown in the Simulink diagram in Figure 9A. The independence of this compensation algorithm in maRTHS, even assuming identical actuators, is proved by Galmez and Fermandois (2022) as the parameter adaptation process is different for each one of the actuators. Figure 9B shows a block diagram of the implemented RoDeAC for virtual maRTHS.

4 Calibration of robust decentralized adaptive compensators

4.1 Initial parameters $P[0]$ and $FF[0]$

Offline tests are required to provide the necessary data for initializing the RLS-AC method and assessing the method's performance for prescribed desired displacement loading. Then, a Simulink implementation is used, as shown in Figure 10, where the structural response is measured in an open-loop system without the feedback of the experimental forces back to the numerical substructure. In this case, we use the multi-actuator models described in Section 2.3.2, which provides information about the

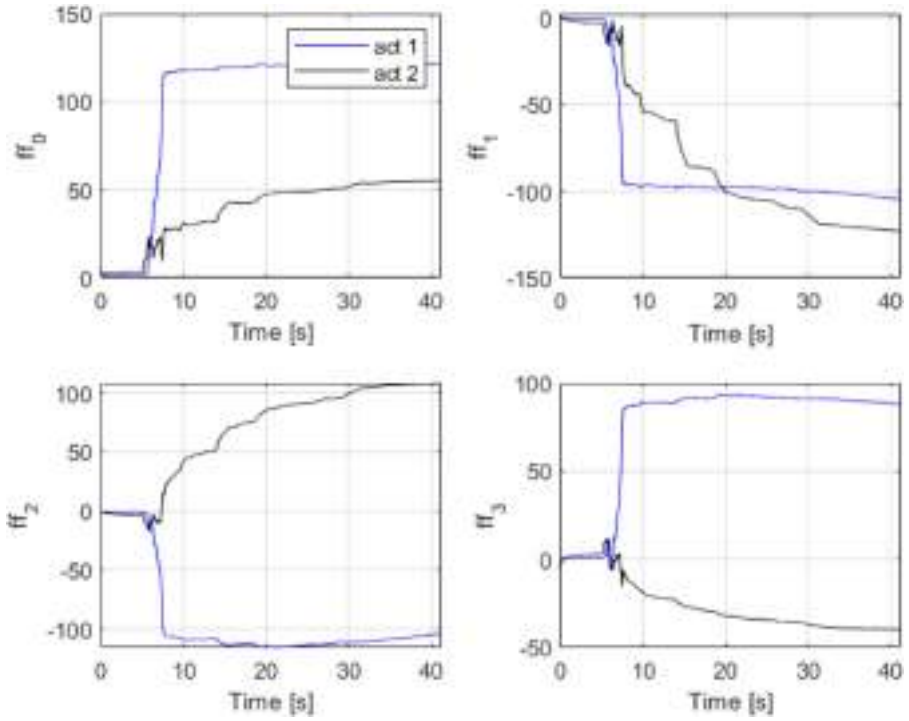

FIGURE 16
Evolution of RoDeAC adaptive parameters for the virtual maRTHS.

control system with the numerical substructure subjected to seismic excitation. Notably, this process can be carried out even without any interaction with the test specimen. Then, the structural response is imposed on the specimen (x_t), and the displacement response is measured (x_m). Finally, the values of the parameters $P[0]$ and $FF[0]$ are obtained using Eqs 15 and 16.

Different scenarios are used to analyze the initial parameters' dispersion for the offline calibration. Therefore, three different earthquakes (El Centro, 1940; Kobe, 1995; and Morgan, 1984) with different seismic intensity measures (20%, 40%, and 60% PGA scales) are used to calculate different $P[0]$ and $FF[0]$ parameters. Furthermore, we considered uncertainty in the control plant as described in Section 2.2.2, with 10 simulations for each combination of earthquake ground motion and intensity measure. The uncertainty propagation in $P[0]$ and $FF[0]$ initial parameters is shown in boxplots in Figures 11, 12.

Note that, under the assumption of different conditions, the values for the initial parameter values change. Moreover, in this case, different values for parameters $P[0]$ and $FF[0]$ are obtained for slightly different actuators modeled as described in Section 2.2.2.

Finally, the mean values are considered in this study for the initialization of each parameter and are presented in Eqs 19–22.

- Actuator 1:

$$P_1[0] = \begin{bmatrix} 83906 & -45046 & -27999 & -10761 \\ -45046 & 106713 & -33590 & -28000 \\ -27999 & -33590 & 106713 & -45047 \\ -10761 & -28000 & -45047 & 83908 \end{bmatrix}, \quad (19)$$

$$FF_1[0] = [5.41 \quad 1.96 \quad -1.5 \quad -4.96]^T. \quad (20)$$

- Actuator 2:

$$P_2[0] = \begin{bmatrix} 64773 & -51448 & -21630 & 8377 \\ -51448 & 104561 & -31474 & -21630 \\ -21630 & -31474 & 104561 & -51449 \\ 8337 & -21630 & -51449 & 64774 \end{bmatrix}, \quad (21)$$

$$FF_2[0] = [6.06 \quad 2.20 \quad -1.67 \quad -5.54]^T. \quad (22)$$

4.2 Forgetting factor

The forgetting factor is used to weaken the influence of older data on the estimated parameter values. This means that as simulation time increases, the old data are discarded exponentially by the parameter estimator of the adaptive compensator (Ioannou and Sun, 2012). A small forgetting factor decreases the impact of older data on the identified parameters and is thus more suitable for time-varying systems. However, small forgetting factors may cause serious fluctuations in the identified parameters (Wang et al., 2020). To observe how this parameter affects our virtual maRTHS, graphs illustrating the J_2 and J_5 error indicators (defined in Appendix A of the Supplementary Material) are presented in Figure 13. As reflected in these graphs, the lowest error is achieved with a fixed value of the forgetting factor $\rho = 1$ since lower values seem to cause instabilities and fluctuations in this approach, indicating that the identified parameters depend heavily on the older data. Therefore, a forgetting factor $\rho = 1$ is adopted in this study.

TABLE 2 Virtual maRTHS evaluation criteria (100 realizations).

Performance criterion	Criterion	Mean performance index	Unit	RTHS–benchmark	vRTHS—benchmark	Proposed RoDeAC
Tracking control	Time delay	$\bar{J}_{1,1}$	ms	−13.7	2.0	0
		$\bar{J}_{1,2}$	ms	2.9	2.9	0
	Normalized tracking error	$\bar{J}_{2,1}$	%	23.8	4.8	3.0
		$\bar{J}_{2,2}$	%	13.2	9.4	1.7
	Maximum peak tracking error	$\bar{J}_{3,1}$	%	26.9	5.3	4.2
		$\bar{J}_{3,2}$	%	13.7	10.3	2.5
Estimation	Time delay	$\bar{J}_{4,1}$	ms	1.9	1.9	0
		$\bar{J}_{4,2}$	ms	4.9	2.9	0
	Normalized estimation error	$\bar{J}_{5,4}$	%	8.1	6.7	2.0
		$\bar{J}_{5,28}$	%	27.8	17.8	2.7
	Maximum peak estimation error	$\bar{J}_{6,4}$	%	8.2	7.4	2.3
		$\bar{J}_{6,28}$	%	28.6	18.8	5
Global RTHS Accuracy	Normalized RTHS error	$\bar{J}_{7,4}$	%	12.2	10.6	9.7
		$\bar{J}_{7,28}$	%	26.2	16.8	7.7
	Normalized RTHS error at upper levels	$\bar{J}_{8,2}$	%	12.5	1.8	6.6
		$\bar{J}_{8,26}$	%	12.7	3.4	5.8
		$\bar{J}_{8,3}$	%	12.4	2.1	6.2
		$\bar{J}_{8,27}$	%	12.5	3	5.9
	Maximum peak RTHS error	$\bar{J}_{9,4}$	%	13.2	11.9	8.3
		$\bar{J}_{9,28}$	%	27.3	18.1	7.1
	Maximum peak RTHS error at upper levels	$\bar{J}_{10,2}$	%	13.1	1.8	4.9
		$\bar{J}_{10,26}$	%	13.4	2.7	4.6
		$\bar{J}_{10,3}$	%	12.8	1.8	4.6
		$\bar{J}_{10,27}$	%	13.2	2.4	4.6

5 Results

The tracking controller was implemented in Simulink using a reference model block provided by the benchmark problem (Condori et al., 2023). Simulations were conducted in real-time using *MATLAB and Simulink* R2021a with *Simulink Desktop Real-Time* version 5.12.0, running on a 64-bit computer with an Intel i7-9750H CPU, 16 GB of RAM, and the Windows 10 version 22H2 operating system. The nominal and 100 perturbed control plants were studied to assess the performance and robustness of the controller employed.

5.1 Compensation of multi-actuator dynamics

To study the tracking performance of the RoDeAC in the time domain, the seismic excitation chosen was the 1940 EL Centro earthquake, with 40% scaled PGA intensity. Figure 14 shows the target (x_t) and measured (x_m) displacements. It can be observed that both target and measured displacements have an excellent match at all simulation times, especially for significant time reversals. In the same way, Figure 15 shows the estimation RTHS accuracy of the interface node. Small differences between calculated and actual signals can be appreciated, which could be attributed to the non-linear nature of the equations for the coupler coordinate transformations or a deficiency in the proposed algorithm. More information on the accuracy of the RoDeAC (measured compared to reference signals) can be found in Appendix B of the Supplementary Material.

Furthermore, Figure 16 presents the evolution of parameter *FF* for each actuator. These results provide evidence of different evolutions in decentralized adaptive compensation and fast adaptation at the beginning of the earthquake (i.e., after 5 [sec]), allowing us to estimate the plant dynamics and achieve reasonable compensation.

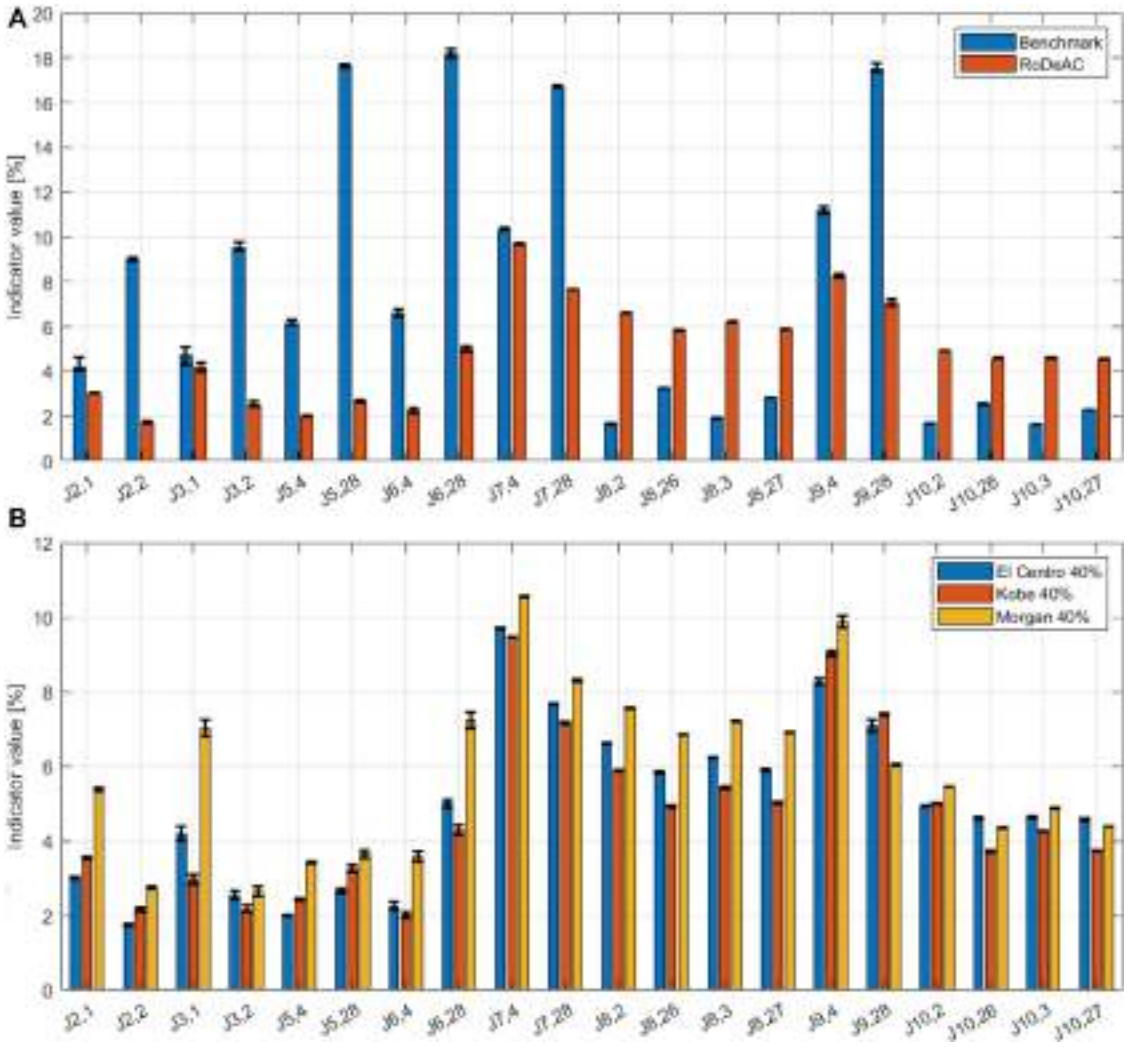

FIGURE 17
Comparison of evaluation criteria between benchmark and RoDeAC with 100 perturbed systems (median and interquartile range): **(A)** El Centro 40% PGA scaled and **(B)** summary of evaluation criteria for the three analyzed earthquakes.

5.2 Evaluation criteria of RoDeAC

To evaluate the accuracy and efficacy of the tracking control, 10 performance indices were defined in the benchmark problem (Condori et al., 2023), which are divided into two groups: (1) the tracking control performance indices and (2) the global RTHS experiment performance indices. The first three criteria (J_1, J_2, and J_3) are measures of the reference tracking properties of the chosen controller, comparing the measured and target displacements. On the other hand, criteria J_4 to J_6 compare the target and commanded displacements. Meanwhile, criteria J_7 to J_{10} establish the error between the measured displacement responses of the hybrid system, compared to the reference structure, at all floor locations of the three-story moment frame. The performance indices J_1 and J_4 have units of time (ms), while the rest are in percentages. Lower scores on all performance indices are desired. Due to the MDOF characteristic of the problem, each performance index is a vector and could be related to the number of the actuator or the node at which it is evaluated. All the equations for the performance indices are included in Appendix A of the Supplementary Material.

Table 2 summarizes the mean calculated indices ($\bar{J}$) of 100 consecutive experiments of the proposed method compared with the values declared in the benchmark problem. It is assumed that 100 realizations are a sufficient sample space for a high return rate and to ensure higher robustness on the problem. Moreover, it should be noticed that some differences were encountered between the uncertainty declared on the benchmark problem and the actual MATLAB codes. Therefore, high instabilities are obtained using the benchmark controller with the stated uncertainty.

The median value of the performance indices of 100 consecutive experiments using RoDeAC, along with the interquartile range, for the El Centro earthquake, scaled to 40% of the PGA intensity, and compared with 100 consecutive experiments with the benchmark controller, are plotted in Figure 17A. Tracking control and estimation indices show that RoDeAC has lower errors than the benchmark controller. For the global RTHS accuracy, the normalized and peak errors are lower at the controlled levels but slightly higher at the upper levels. Along with its high level of robustness, RoDeAC demonstrates excellent overall performance. More information on the performance comparison of the RoDeAC with the

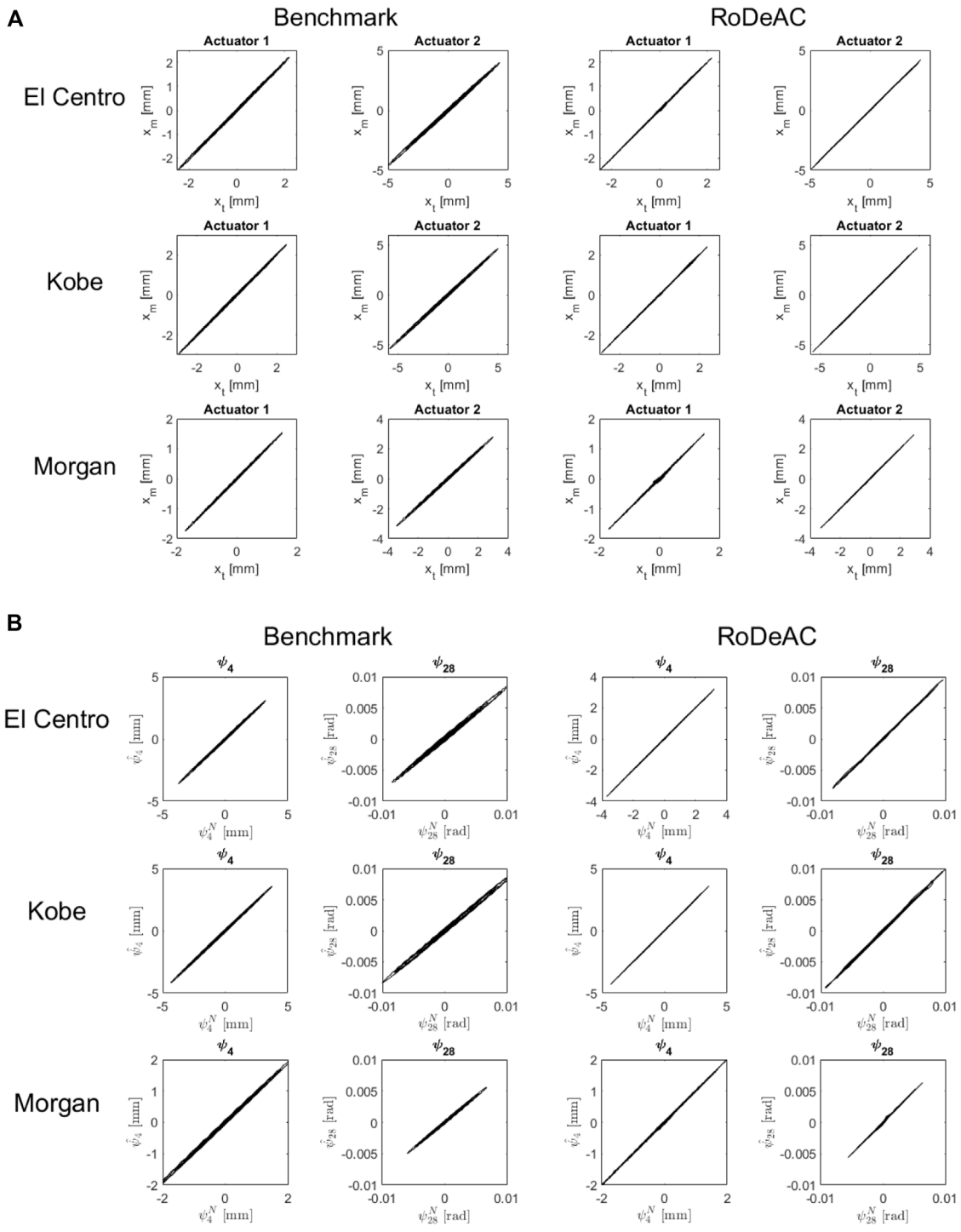

FIGURE 18
Synchronization subspace plots for benchmark and RoDeAC controllers (nominal plant): **(A)** actuator coordinates and **(B)** Cartesian coordinates ψ_4 and ψ_{28}.

benchmark controller for other ground motions can be found in Appendix B of the Supplementary Material. Finally, Figure 17B summarizes the performance indices for the proposed RoDeAC, showing the controller's stable and consistent behavior for the three chosen earthquakes and with 100 different perturbations of the control plant. In particular, the worst performance indices were obtained from the Morgan earthquake with 40% PGA.

On the other hand, the synchronization subspace plots (SSPs) of displacements comparing the benchmark and RoDeAC controllers are shown in Figure 18 for all three earthquakes as inputs of the systems scaled to 40% of the PGA intensity. This visualization allows us to directly compare the system's synchronization, where a straight line with a 1:1 slope represents a perfect synchronization. The plots show that the best synchronization is achieved for the RoDeAC controller in all cases with

thinner SSPs. Nevertheless, the Cartesian SSPs show slightly worse tracking performance compared with the actuator SSPs, especially for the rotation degree of freedom.

6 Conclusion

A robust decentralized adaptive compensator (RoDeAC) was proposed and examined through the next-generation multi-axial real-time hybrid simulation (maRTHS) benchmark problem. In particular, the reference structure corresponds to a three-story, three-bay planar frame where one central frame is the experimental substructure and the rest is the numerical substructure. Displacement and rotation are commanded as target signals at the interface between substructures. Two almost identical actuators are utilized to impose the numerical response; therefore, displacement and rotation are transformed into actuator coordinates to obtain one target signal for each actuator. Then, a decentralized recursive least squares adaptive compensator is employed over the multi-actuator loading assembly. In the virtual implementation, the actuator dynamics are modeled as a family of frequency response function (FRF) models with random parameters to consider actual uncertainty properly during experimental testing. The simulations show excellent tracking results for maRTHS tests and proper robustness even against the uncertainties in the modeled control plant for the three considered earthquake ground motions. It should be noticed that the relatively easy calibration algorithm required for the RoDeAC enables faster implementation of a compensation algorithm, even for more complex problems with a higher number of actuators. Future studies will consider the effect of sampling time and size on the RLS adaptive compensator, and experimental validation of this framework will be conducted on a physical testbed.

Data availability statement

The models and datasets presented in this study can be found in the following online repository: https://github.com/FermandoisLab/maRTHS-bmk-RoDeAC.

Author contributions

MQ: writing–review and editing, writing–original draft, visualization, validation, software, methodology, investigation, formal analysis, data curation, and conceptualization. CG: writing–review and editing, validation, software, resources, methodology, and conceptualization. GF: writing–review and editing, validation, supervision, resources, methodology, and conceptualization.

Funding

The author(s) declare that financial support was received for the research, authorship, and/or publication of this article. This research was supported by *Agencia Nacional de Investigación y Desarrollo* (ANID, Chile) through the Fondecyt Iniciacion Grant No. 11190774.

Conflict of interest

The authors declare that the research was conducted in the absence of any commercial or financial relationships that could be construed as a potential conflict of interest.

Publisher's note

All claims expressed in this article are solely those of the authors and do not necessarily represent those of their affiliated organizations, or those of the publisher, the editors, and the reviewers. Any product that may be evaluated in this article, or claim that may be made by its manufacturer, is not guaranteed or endorsed by the publisher.

Supplementary material

The Supplementary Material for this article can be found online at: https://www.frontiersin.org/articles/10.3389/fbuil.2024.1394952/full#supplementary-material

References

Asai, T., Chang, C. M., Phillips, B. M., and Spencer, B. F. (2013). Real-time hybrid simulation of a smart outrigger damping system for high-rise buildings. *Eng. Struct.* 57, 177–188. doi:10.1016/j.engstruct.2013.09.016

Botelho, R. M., and Christenson, R. E. (2014). Mathematical framework for real-time hybrid substructuring of marine structural systems. *Conf. Proc. Soc. Exp. Mech. Ser.* 4 (February), 175–185. doi:10.1007/978-3-319-04546-7_21

Carrion, J. E., and Spencer, B. F. (2007). Model-based strategies for real-time hybrid testing. Newmark Structural Engineering Laboratory Report Series No. 006. Urbana, IL: Department of Civil and Environmental Engineering, University of Illinois at Urbana-Champaign. URL: http://hdl.handle.net/2142/3629.

Chae, Y., Kazemibidokhti, K., and Ricles, J. M. (2013). Adaptive time series compensator for delay compensation of servo-hydraulic systems for real-time hybrid simulation. *Earthq. Eng. Struct. Dyn.* 42, 1967–1715. doi:10.1002/eqe.2294

Chen, C., and Ricles, J. M. (2010). Tracking error-based servohydraulic actuator adaptive compensation for real-time hybrid simulation. *J. Struct. Eng.* 136 (4), 432–440. doi:10.1061/(ASCE)ST.1943-541X.0000124

Chen, P. C., Chang, C. M., Spencer, B. F., and Tsai, K. C. (2015). Adaptive model-based tracking control for real-time hybrid simulation. *Bull. Earthq. Eng.* 13 (6), 1633–1653. doi:10.1007/s10518-014-9681-2

Condori, J. W., Salmeron, M., Patino, E., Montoya, H., Dyke, S. J., Silva, C. S., et al. (2023). Experimental benchmark control problem for multi-axial real-time hybrid simulation. *Front. Built Environ.* 9. doi:10.3389/fbuil.2023.1270996

Dermitzakis, S. N., and Mahin, S. A. (1985). Development of substructuring techniques for on-line computer controlled seismic performance testing. Report No. UCB/EERC-85/04. Berkeley, California: Earthquake Engineering Research Center, University of California.

Fermandois, G. A., and Spencer, B. F. (2017). Model-based framework for multi-axial real-time hybrid simulation testing. *Earthq. Eng. Eng. Vib.* 16 (4), 671–691. doi:10.1007/s11803-017-0407-8

Galmez, C., and Fermandois, G. (2022). "Recent developments on robust adaptive compensation in multi-axial real-time hybrid simulation," in Proceedings of the 8th World Conference on Structural Control and Health Monitoring, Orlando, FL, 5-8 June, 2022.

Ghaffary, A., and Mohammadi, R. K. (2019). Comprehensive nonlinear seismic performance assessment of MR damper controlled systems using virtual real-time hybrid simulation. *Struct. Des. Tall Special Build.* 28 (8), 1–18. doi:10.1002/tal.1606

Horiuchi, T., Inoue, M., Konno, T., and Namita, Y. (1999). Real-time hybrid experimental system with actuator delay compensation and its application to a piping system with energy absorber. *Earthq. Eng. Struct. Dyn.* 28 (10), 1121–1141. doi:10.1002/(SICI)1096-9845(199910)28:10<1121::AID-EQE858>3.0.CO;2-O

Horiuchi, T., Nakagawa, M., Sugano, M., and Konno, T. (1996). Development of a real-time hybrid experimental system with actuator delay compensation. Proc. of 11th World Conf. Earthquake Engineering, Acapulco, Mexico, June 23–28.

Ioannou, P. A., and Sun, J. (2012). *Robust adaptive control*. Mineola, NY: Dover Publications.

Najafi, A., Fermandois, G. A., Dyke, S. J., and Spencer, B. F. (2023). Hybrid simulation with multiple actuators: a state-of-the-art review. *Eng. Struct.* 276 (2022), 115284. doi:10.1016/j.engstruct.2022.115284

Najafi, A., Fermandois, G. A., and Spencer, B. F. (2020). Decoupled model-based real-time hybrid simulation with multi-axial load and boundary condition boxes. *Eng. Struct.* 219 (May), 110868. doi:10.1016/j.engstruct.2020.110868

Nakashima, M., Kato, H., and Takaoka, E. (1992). Development of real-time pseudo dynamic testing. *Earthq. Eng. Struct. Dyn.* 21 (1), 79–92. doi:10.1002/eqe.4290210106

Ning, X., Wang, Z., and Wu, B. (2020). Kalman filter-based adaptive delay compensation for benchmark problem in real-time hybrid simulation. *Appl. Sci.* 10 (20), 7101. doi:10.3390/app10207101

Palacio-Betancur, A., and Gutierrez Soto, M. (2019). Adaptive tracking control for real-time hybrid simulation of structures subjected to seismic loading. *Mech. Syst. Signal Process.* 134, 106345. doi:10.1016/j.ymssp.2019.106345

Phillips, B. M., and Spencer, B. F., Jr. (2012). Model-based framework for real-time dynamic structural performance evaluation. Newmark Structural Engineering Laboratory Report Series No. 031. University of Illinois at Urbana-Champaign 31 (August), 46–59. URL: http://hdl.handle.net/2142/33794.

Silva, C. E., Gomez, D., Amin, M., Dyke, S. J., and Spencer, B. F. (2020). Benchmark control problem for real-time hybrid simulation. *Mech. Syst. Signal Process.* 135, 106381. doi:10.1016/j.ymssp.2019.106381

Söderström, T., and Stoica, P. (1988). *System identification*. United States: Prentice-Hall, Inc.

Tao, J., and Mercan, O. (2019). A study on a benchmark control problem for real-time hybrid simulation with a tracking error-based adaptive compensator combined with a supplementary proportional-integral-derivative controller. *Mech. Syst. Signal Process.* 134, 106346. doi:10.1016/j.ymssp.2019.106346

Wang, Z., Guoshan, Xu, Qiang, Li, and Bin, Wu (2020). An adaptive delay compensation method based on a discrete system model for real-time hybrid simulation. *Smart Struct. Syst.* 25 (5), 569–580. doi:10.12989/sss.2020.25.5.569

Xu, W., Chen, C., Guo, T., and Chen, M. (2019). Evaluation of frequency evaluation index based compensation for benchmark study in real-time hybrid simulation. *Mech. Syst. Signal Process.* 130, 649–663. doi:10.1016/j.ymssp.2019.05.039